Biomechanics of porcine renal arteries and role of axial stretch.

Stéphane Avril, Pierre Badel, Mohamed Gabr, Michael Sutton, Susan Lessner

▶ To cite this version:

HAL Id: hal-00834145

https://hal.archives-ouvertes.fr/hal-00834145

Submitted on 6 Aug 2013

Biomechanics of porcine renal arteries and role of axial stretch

Stéphane Avril[1], Pierre Badel[1], Mohamed Gabr[2],

Michael A. Sutton[2,3], Susan M. Lessner[2,4]

[1]Ecole Nationale Supérieure des Mines, CIS-ENSMSE, CNRS:UMR5146, F-42023 Saint-Etienne

[2]Biomedical Engineering Program, School of Medicine, University of South Carolina, Columbia, SC 29208

[3]Department of Mechanical Engineering, University of South Carolina, Columbia, SC 29208

[4]Department of Cell Biology and Anatomy, School of Medicine, University of South Carolina, Columbia, SC 29208

Abstract

It is known that arteries experience significant axial stretches *in vivo*. Several authors have shown that the axial force needed to maintain an artery at its *in vivo* axial stretch does not change with transient cyclical pressurization over normal ranges. However, the axial force phenomenon of arteries has never been explained with microstructural considerations. In this paper, we propose a simple biomechanical model to relate the specific axial force phenomenon of arteries to the predicted load-dependent average collagen fiber orientation. It is shown that (a) the model correctly predicts the authors' experimentally measured biaxial behaviour of pig renal arteries and (b) the model predictions are in agreement with additional experimental results reported in the literature. Finally, we discuss the implications of the model for collagen fiber orientation and deposition in arteries.

Key terms

Biomechanics; Arterial wall; axial stretch; anisotropy; biaxial testing; modelling; collagen fibers; law of mixtures, inverse identification.

1. Introduction

It is known that arteries experience significant axial stretches *in vivo* [14, 16, 24, 25]. According to Humphrey et al. [16], the axial component of wall stress plays a fundamental role in controlling arterial geometry, structure, and function. Given the explosion of interest in mathematical modeling of arterial growth and remodeling [4, 8, 12, 17, 19, 24], the fundamental role of axial wall stress has been investigated in conceptual and theoretical models of arterial growth and remodeling [7, 8, 16, 29].

The most important result in the literature regarding the role of axial stretch in arteries is that the axial force needed to maintain an artery at its *in vivo* axial stretch does not change with transient cyclical pressurization over normal ranges [1, 3, 5, 15, 24, 25]. This is a very interesting phenomenon and the specific biaxial behaviour of blood vessels has received much attention by numerous authors [20, 22, 23, 26].

Although mathematical models considering the three primary structural constituents of arterial walls (elastin, collagen, and smooth muscle) are now able to predict arterial anisotropy and residual stresses [4, 17, 21], to the authors' knowledge, conceptual understanding of the *in vivo* axial force phenomenon has not been explained through the use of biomechanical models.

In this paper, we propose a biomechanical model based on the law of mixtures to relate the specific biaxial behaviour of arteries to the predicted load-dependent average collagen fiber orientation. It is shown that the model correctly predicts both (a) the authors' experimentally measured biaxial behaviour of pig renal arteries and (b) additional experimental results

reported in the literature regarding the biaxial behaviour of arteries. Finally, we discuss the implications of this model for collagen fiber orientation and deposition in arteries.

2. Material and methods

2.1 Model for predicting axial load and internal pressure in arteries

The objective of this paper is to focus on the relationship between the axial force and the internal pressure applied to a cylindrical segment of an artery (Fig. 1). The basic equation of equilibrium for a cylindrical tube subjected to the combined loading of axial load and internal pressure is:

$$F_z = 2\pi \int_{r_i}^{r_o} \sigma_{zz}(r) r \, dr - \pi \, r_i^2 \, P \tag{1}$$

where F_z is the measured axial force, called *reduced axial force* [12]; r_o and r_i are respectively the current outer and inner radii of the cylinder in the deformed configuration; σ_{zz} is the axial stress in the wall; and P is the pressure inside the artery (the pressure outside is neglected).

The internal pressure may be related to the circumferential and radial stress in the arterial wall as follows:

$$P = \int_{r_i}^{r_o} [\sigma_{\theta\theta}(r) - \sigma_{rr}(r)] \frac{dr}{r} \tag{2}$$

where $\sigma_{\theta\theta}$ and σ_{rr} are respectively the circumferential and radial stresses in the wall.

An arterial wall is constructed of a network of collagen fibers and smooth muscle cells reinforcing an amorphous matrix [15]. The microstructure of the arterial tissue is very complex and it is preferred to represent it by an equivalent material model.

In this study, the equivalent material model is based on the law of mixtures. It neglects the mechanical contribution of the amorphous matrix and considers four families of parallel fibers [27, 28] aligned in preferred directions that are oriented at an angle, Φ, relative to the circumferential direction (Fig. 2). Conceptually, the fiber model shown in Fig. 2 supports loads (hence, stresses) mainly along the fiber directions. The tensile/compressive stress in the fibers is denoted σ_Φ. The four angles are $\Phi = 0°$, $\Phi = 90°$, $\Phi = +\beta$ and $\Phi = -\beta$. The fiber families at $\Phi = +\beta$ and $\Phi = -\beta$ represent helically distributed fibers (see schematic in Fig. 1) which are known to be responsible for coupling effects between circumferential and axial stresses [12].

Assuming that the fibers at angle $+\beta$ and $-\beta$ contribute similarly to the arterial stresses $\sigma_{\theta\theta}$ and σ_{zz} so that ρ_β denotes the sum of volume fractions of fibers at $+\beta$ and $-\beta$, the stresses in the circumferential and axial directions within the arterial wall are determined in terms of stresses in the fibers at orientation Φ and the volume fraction of fibers (see details in the Appendix):

$$\sigma_{\theta\theta} - \sigma_{rr} = \rho_\beta \, \sigma_\beta \, \cos^2(\beta) + \rho_0 \, \sigma_0 \tag{3}$$

$$\sigma_{zz} - \sigma_{rr} = \rho_\beta \, \sigma_\beta \, \sin^2(\beta) + \rho_{90} \, \sigma_{90} \tag{4}$$

where ρ_Φ denotes the volume fraction of the fibers oriented at angle Φ.

Assuming incompressibility and neglecting shear in the tension/inflation tests, the following deformation gradient tensor (from the stress-free configuration to the loaded state) written in cylindrical coordinates is used to describe the artery deformation state:

$$[\underline{\underline{F}}] = \begin{bmatrix} \lambda_\theta^{-1}\lambda_z^{-1} & 0 & 0 \\ 0 & \lambda_\theta & 0 \\ 0 & 0 & \lambda_z \end{bmatrix} \tag{5}$$

where λ_θ and λ_z are, respectively, the stretches in the circumferential and axial directions. Uniform deformation of the cylindrical artery is assumed for the axial stretch. Radial variations of λ_θ are considered, satisfying:

$$\lambda_\theta(R) = \frac{1}{R}\frac{2\pi}{2\pi-\alpha}\sqrt{\frac{R^2-R_i^2}{\lambda_z}\frac{2\pi-\alpha}{2\pi}+r_i^2} \tag{6a}$$

where R is the radial coordinate in the reference undeformed configuration, R_i is the inner radius in the reference undeformed configuration, α is the opening angle [5] in radian relating the traction-free to the stress-free state (the definition of the opening angle for an open sector of artery is shown in Fig. 3). Note that, in practice, we measure the outer radius r_o, and the inner radius is deduced under the assumption of incompressibility according to:

$$r_o^2 - r_i^2 = \frac{R_o^2-R_i^2}{\lambda_z}\frac{2\pi-\alpha}{2\pi} \tag{6b}$$

In this study, it is assumed that the fibers are hyperelastic with an exponential strain energy function (equation A6), yielding the following relationships between σ_β, σ_{90} and σ_0 and the stretch ratios;

$$\rho_\beta \, \sigma_\beta = k_{\beta 1}(\lambda_{\beta 0}{}^2 - 1) \, \exp[k_{\beta 2}(\lambda_{\beta 0}{}^2 - 1)^2] \, \lambda_{\beta 0}{}^2 \tag{7}$$

$$\rho_{90} \, \sigma_{90} = k_{901}(\lambda_z{}^2 - 1) \, \exp[k_{902}(\lambda_z{}^2 - 1)^2] \, \lambda_z{}^2 \tag{8}$$

$$\rho_0 \, \sigma_0 = k_{01}(\lambda_\theta{}^2 - 1) \, \exp[k_{02}(\lambda_\theta{}^2 - 1)^2] \, \lambda_\theta{}^2 \tag{9}$$

where $k_{\beta 1}$, $k_{\beta 2}$, k_{901}, k_{902}, k_{01} and k_{02} are material parameters and $\lambda_{\beta 0}$ is the stretch of the helical fibers (see details in the Appendix)

Combining Eqs (2), (3), (7) and (9), the internal pressure predicted by the model can be written in the following form;

$$\widetilde{P} = \int_{r_i}^{r_o} \left[k_{\beta 1}\lambda_\theta^2 \cos^2(\beta_0)\left(\lambda_{\beta_0}^2 - 1\right)\exp\left(k_{\beta 2}\left(\lambda_{\beta_0}^2 - 1\right)^2\right) + k_{01}\lambda_\theta^2\left(\lambda_\theta^2 - 1\right)\exp\left(k_{02}\left(\lambda_\theta^2 - 1\right)^2\right) \right]\frac{dr}{r} \tag{10}$$

Combining Eqs (1), (4), (7) and (8), the axial force predicted by the model can be written in the following form;

$$\widetilde{F}_z = \widetilde{F}_0(\lambda_z) + \int_{r_i}^{r_o} 2\pi\left[k_{\beta 1}\lambda_z^2 \sin^2(\beta_0)\left(\lambda_{\beta_0}^2 - 1\right)\exp\left(k_{\beta 2}\left(\lambda_{\beta_0}^2 - 1\right)^2\right)\right] r\,dr - P\pi r_a^2 \tag{11}$$

Where r_a is defined in the appendices (Eq. A22) and $\widetilde{F}_0(\lambda_z)$ is a term which depends on λ_z only and not on P ($\widetilde{F}_0$ is the value of $\widetilde{F}_z$ at P=0):

$$\widetilde{F}_0(\lambda_z) = 2\pi\int_{r_i}^{r_o} \left\{ k_{901}\lambda_z^2\left(\lambda_z^2 - 1\right)\exp\left(k_{902}\left(\lambda_z^2 - 1\right)^2\right) \right\} r\,dr \tag{12}$$

In the following, $\widetilde{F}_z - \widetilde{F}_0$ will be designated $\widetilde{F}$. Note that Eq (11) is able to predict the F-P relationship from the knowledge of the current outer diameter and length and that it only depends on the orientation angle and material properties of the helical fibers.

Eventually, the proposed material equivalent model has 8 parameters to be determined:

- the opening angle: α

- the orientation angle of helical fibers in the stress-free state: β_0

- the stiffness property of the helical fiber: $k_{\beta 1}$

- the exponential stiffening coefficient of the helical fibers: $k_{\beta 2}$

- the stiffness property of the circumferential fibers: k_{01}

- the exponential stiffening coefficient of the circumferential fibers: k_{02}.

- the stiffness property of the axial fibers: k_{901}

- and the exponential stiffening coefficient of the axial fibers: k_{902}.

The opening angle is measured experimentally (section 2.2).

The identification of the other material parameters is achieved in 3 stages:

1. First, we identify β_0, $k_{\beta 1}$ and $k_{\beta 2}$ by calibrating equation (11) against experimental F-P data.

2. Second, we identify k_{01} and k_{02} by calibrating equation (10) against experimental P data. Equation 10 also involves β_0, $k_{\beta 1}$ and $k_{\beta 2}$ but they have already been identified at stage 1.

3. Third, we identify k_{901} and k_{902} by calibrating equation (12) against experimental F_0 data (axial tensile tests at zero pressure).

The identification is achieved by maximizing the coefficient of determination R^2 which is defined such as:

$$R^2 = 1 - \frac{\sum_{i=1}^{n}\left(Y_i - \tilde{Y}_i\right)^2}{n\sigma_Y^2} \qquad (13)$$

where Y_i is a measurement (F at stage 1, P at stage 2), $\tilde{Y}_i$ is the model prediction ($\tilde{F}$ predicted by Eq. (11) at stage 1, $\tilde{P}$ predicted by Eq. (10) at stage 2), n is the number of measurements and σ_Y is the standard deviation of the measurements.

2. 2.   Experiments on porcine artery specimens

Pairs of porcine kidneys attached to intact abdominal aortic segments were acquired post-mortem from a local processing facility in Lexington, SC. Based on information provided by the facility, the specimens were obtained from 2-3 yr old sows (weight range approx. 159-205 kg). After removal from the carcass, the arterial specimens remained immersed in solution until the mechanical loading process was completed; all experiments were performed within a few hours of tissue removal from the pig. When detaching the porcine renal and first branch specimens from the kidneys, the *in situ* axial and circumferential stretches were estimated through measurement of (a) the axial contraction of the artery specimen during removal and (b) the final outer diameter of the artery specimen after removal. Opening angle α was also measured from cylindrical ring specimens cut from the artery after its removal.

To obtain an estimate for the *in situ* axial stretch, markers were placed on the renal artery specimen at a few locations along the length. Then, with a ruler in the field of view, a camera was placed perpendicular to the renal artery and an image of the specimen and ruler was acquired prior to excision. After excision, another image was acquired of the specimen

9

without altering the camera settings and with a ruler again in the field of view. Using these images, post-processing was performed to obtain estimates for the stretch ratio between the markers. The average of all stretch ratios is used in our studies.

To obtain an estimate for the *in situ* circumferential stretch ratio, the same images were again post-processed. Here, the diameter of the vessel was obtained by post-processing of the images at several clearly identifiable locations along the vessel, before and after excision. Finally, the data is used to obtain estimates for the circumferential stretch ratio at several locations, with the average used in our studies.

Mechanical testing using both pressurization and axial loading was carried out on a Bose Electroforce Biodynamic 5100 Test Bench (Bose, Eden Prairie, MN). The Bose Test Bench includes (a) 22N load cell, (b) micro-pump capable of delivering 102ml/min, (c) catheter-mounted pressure sensor with a range of 0-300mm Hg, (d) actuator that can produce a total displacement of 13mm, (e) environmental chamber to maintain hydration of the arterial specimens (Fig. 4A) and (f) Bose software to control the entire mechanical loading process.

To perform the experiments, each arterial specimen was mounted to hollow cylindrical, barb-ended Luer stubs (McMaster-Carr) using 3-0 silk sutures. After the specimen was sutured onto the Luer stubs, the stub-artery combination was attached to the end fixtures of the Bose Test Bench and immersed in a bath of 1X phosphate-buffered saline (PBS) solution within the environmental chamber (see Fig. 4B). The specimen was immediately perfused internally with the same solution at room temperature and perfusion was maintained throughout the loading process.

Arterial specimens were pre-conditioned mechanically by 5 cycles of stretching to 3.5% beyond the traction-free length, L_0. Then, experiments were performed at a constant perfusion rate over the range $20\text{mmHg} \leq P \leq 140\text{mmHg}$, while maintaining a constant axial stretch ratio in the range encompassing $1.00 \leq \lambda_z \leq 1.25$. To determine the axial stretch ratio, the initial (undeformed) length was defined to be the specimen length between the sutured ends when the axial load is zero.

During the mechanical loading process, the deformed outer diameter and length of the specimen were determined at each loading step by analyzing images of the specimen. In this study, all images were acquired using a Grasshopper 50S5M 5.0 megapixel CCD camera (Point Grey, Richmond, BC) with a 28mm Nikon lens. Image acquisition was performed using Vic-Snap 2010 Software (Correlated Solutions, Columbia, SC). The images were analyzed using ImagePro Plus 7 image analysis software (Media Cybernetics, McClean, VA) to determine the average deformed diameter in the central region and the deformed length. To obtain the axial and circumferential strains during the mechanical experiment, the procedures outlined above for measurement of *in situ* dimensions were essentially repeated at each load step to determine the current diameter and current length at selected marker positions along the length. These were then used with the reference values to obtain an average axial stretch ratio and average circumferential stretch ratio.

Ten segments of pig renal arteries from five different pigs were tested using this protocol. Five segments came from the right renal artery (RRA) of the pigs, one from the left renal artery (LRA) and four others came from the left segmental artery (LSA) of the pigs, which is the first branch of the renal artery entering the kidney.

3. Results

Equations (10) and (11) present a model for the biomechanical behaviour of arteries subjected simultaneously to the actions of an axial force and internal pressure. For example, with knowledge of λ_z and $\lambda_\theta(R_i)$, typical graphs of $\tilde{P}$ can be obtained (Eq. 10) and with knowledge of λ_z, $\lambda_\theta(R_i)$ and P, typical graphs of $\tilde{F}$ can be obtained (Eq. 11). The computations are performed in Matlab where the integrals of Equations (10) and (11) have been discretized.

Table 1 presents a summary of the artery measurements for all specimens. The traction-free outer diameter of the main renal artery is significantly greater that that of its first branch (segmental artery), 7.8±1.1 mm vs. 5.1±0.6 mm (two-tailed t-test, P < 0.01), as expected in a diverging, branched arterial tree. In addition, the arterial wall in the stress-free reference configuration is significantly thicker in the main renal artery than in the first branch vessel (1.5±0.4 mm vs. 1.1±0.1 mm, P=0.045, 1-tailed t-test). Measured opening angles were not significantly different between the main renal artery and the first segmental artery.

The identified values for all the parameters of this model are reported in Table 2. It should be noted that the small number of specimens and the large variability among samples did not allow us to identify any statistically significant differences in fitted parameters between the main renal artery and its first branch. In particular, the fitted fiber angle parameter, β_0, was not significantly different between the main renal artery and the first branch vessel (40°±30° vs. 47°±28°, NS). It is emphasized that the β_0 value, along with the $k_{\beta1}$ and $k_{\beta2}$ parameters, has been identified by calibrating the model given in Eq (11) against the experimental F-P curves. The k_{01} and k_{02} parameters have been identified by calibrating the model given in Eq (10) against the experimental P curves. The coefficients of determination R^2 of both

calibrations are reported in Table 2. A perfect fit corresponds to $R^2=1$. Six out of 10 F-P fits have a coefficient of determination larger than 0.7 which shows that our model is able to reproduce very satisfactorily the F-P behaviour of the arteries. For the same arteries, the prediction of the P curves also has fairly good coefficients of determination.

Parameters k_{901} and k_{902} were identified from the values of the axial load at the beginning of each pressure controlled test. Coefficients of determination larger than 0.75 are obtained for 9 out of 10 samples (Tab 2) for the identification of k_{901} and k_{902}.

Figure 5 presents a direct comparison of the F-P measurements from two of our porcine artery experiments for various values of axial stretches, λ_z, and model predictions using Eq (11). As shown in Fig. 5, there is very good to excellent agreement between the experimental data and theoretical predictions for the porcine renal artery specimens.

Figure 6 presents a direct comparison of the P measurements from the same porcine artery experiments for various values of λ_θ ratios, and model predictions using Eq (10). As shown in Fig. 6, there is also good agreement between the experimental data and theoretical predictions.

Figure 7 presents a direct comparison of the axial stress measurements (ratio between the measured values of F_0 and the current cross section area of the vessel wall) from the same porcine artery experiments for various values of λ_z ratios, and model predictions using Eq (12). There is also very good agreement between the experimental data and theoretical predictions.

4. Discussion

4.1. The typical F-P behaviour of arteries

Typical experimental F-P curves for arteries have been reported in many scientific papers [1, 3, 5, 15, 24, 25]. These curves generally have the shape which is displayed in Fig. 5 by our recent experimental results and model predictions. It is noted that, depending upon the axial stretch λ_z, the slope dF/dP may be negative or positive. Most importantly, there is always an axial stretch λ_z for which dF/dP=0.

This specific F-P behaviour is actually a consequence of the presence of helical fibers as shown in our equivalent material model. This is an original result because, while several scientific papers have reported the existence of an axial stretch for which dF/dP = 0, the connection of this observation to the orientation angle of the helically arranged fibers of an equivalent material model has not previously been reported.

This result is not restricted to our experimental data. For instance, as shown in Fig. 8, Hu et al. [14] reported F-P curves for a pig basilar artery. Also shown in Fig. 8 are the predicted trends using Eq (11), where it is clear that the experimental trends of Hu et al [14] are predicted by the model. The β_0 value of the model used for plotting the curves of Fig. 8 is 32.6°.

4.2. Specific cases

In our model, we considered four families of fibers, but the results reported in Tab. 2 show that for 7 out of 10 specimens, the F and P experimental data can be reproduced by the model

without using the circumferential fibers in the model ($k_{01}=0$). This is the case for instance of RRA pig ID#5 for which the F and P curves are shown in Fig. 5 and Fig. 6.

In this specific case, Eq. 4 may be rewritten:

$$\sigma_{zz} - \sigma_{rr} = \sigma_{\theta\theta} \tan^2(\beta) + \rho_{90} \, \sigma_{90} \tag{14}$$

Note that β is the current orientation angle and it is related to the orientation angle β_0 in the stress free state according to rotation equations which are detailed in Appendix.

Our model was devised for thick-walled membranes as the radius/thickness ratio is less than 5. However, it is interesting to consider the F-P relationship in the membrane approximation ($h<<r_i$) as this approximation may be satisfied for larger arteries. In this case, a single radial position is used for estimating $\sigma_{\theta\theta}$ and σ_{rr}, conventionally r_i and it may be written:

$$P \approx \sigma_{\theta\theta}(r_i) \, h/r_i \quad \text{and} \quad \sigma_{rr}(r_i) \approx 0 \tag{15}$$

Combining Eqs (14) and (15) into Eq (1), one may find an interesting F-P relationship for thin-walled arteries having only helical fibers oriented at an angle $0°< \beta<90°$:

$$F \approx \pi r_i^2 P\left(2\tan^2(\beta) - 1\right) \tag{16}$$

Even though Eq. (16) is only satisfied under very specific assumptions, it is worth noting that the only combination of (F, P) for which dF/dP=0 is, as previously introduced by Badel et al. [2]:

15

$$\beta = \tan^{-1}\left(\sqrt{\frac{1}{2}}\right) = 35.3°$$

(17)

This means that an average angle $\beta \approx 35.3°$ is required for observing dF/dP=0 in the specific case of thin-walled arteries having only helical fibers oriented at an angle $0° < \beta < 90°$.

4.3.   Implications on the orientation and deposition of collagen fibers through remodeling processes

We have shown that the specific F-P behavior of arteries can be fully explained by the presence of helical fibers which induce a coupling between circumferential and axial stresses. Even if in reality they are not all aligned along a single direction, helical fibers have already been observed in arteries. For instance, Haskett et al. [10] measured fiber alignment for the human aorta using small angle light scattering (SALS). However their conclusion was that the regression fit of tensile curves predicted different fiber alignment angles than those measured by SALS. Comparison with a direct observation of the histological microstructure using micrographs may be more in agreement with the mechanical predictions [13]. Measurement of fiber alignment angles using multiphoton microscopy is another promising alternative [11].

Our prediction for some specific arteries that an angle $\beta \approx 35.3°$ yields dF/dP=0 is in agreement with the fact that collagen fiber angles in this range have also been observed *in situ* [13].

Accordingly, the presence of helical fibers oriented in this range *in vivo* may explain why it is supposed by several authors [1, 3, 5, 15, 24, 25] that the axial force *in vivo* remains almost

constant in similar arteries over the normal range of physiologic pressures. However, more precise comparison with actual histological microstructures should be achieved, and future work in our laboratories will include histological measurements to improve understanding regarding this issue.

The impact of our result is important for predicting the deposition of collagen fibers. Indeed, if dF/dP=0 represents a normal configuration for the artery *in vivo*, this can be reached by the deposition of collagen fibers at a certain angle to the circumferential direction. Several scientific papers have reported that remodeling processes may act on the deposition of collagen fibers [9] and that axial stresses may affect these remodeling processes. This view is fully consistent with our model.

4.4.　　　Identification of the k_{901} and k_{902} parameters

Parameters k_{901} and k_{902} were identified from the values of F_0 at the beginning of each pressure controlled test. Even though the data results in very good R^2 values (see Tab. 2, last column) and very good curve fitting agreement (Fig 7), in general the identification should be carried out with a separate axial tensile test at a controlled zero pressure before doing the other pressure controlled tests. Though the separate axial tensile test was not performed in the current study despite this limitation, the model accurately predicts the incremental variations of axial loads in arteries when pressures and axial stretches vary. In principle, the model should be restricted to such incremental predictions before separate axial tensile experiments are performed in future studies.

4.5.　　　Limitations and future improvements

Arteries are usually made up of several layers, and Eq (11) is a monolayer model averaging the effects of the various layers. Therefore, in order to be more complete, multilayer modeling should be considered and scatter in the fiber orientation angles should also be introduced into the model [6]. Moreover, since collagen is initially crimped and gradually becomes engaged as the vessel stretches, this effect should play a role in the reorientation of the fibers but it is not taken into account in our model. Considering gradual fiber recruitment [11] is a promising improvement to be considered.

Separate experiments, such as uniaxial and biaxial loading, could also be performed on the media and on the adventitia of arteries [18] to identify the properties of the individual layers, though this was not done in our porcine renal artery experiments.

Models in the literature usually consider the contribution of the amorphous matrix in the artery through a Neo-Hookean hyperelastic potential [12]. This was neglected in the final expression of the Cauchy stress in our model (Eq. A16). It was verified a posteriori that varying the Neo-Hookean parameter values within normal ranges for this parameter ($0 < c < 100$ kPa [4, 12, 13]) does not affect the F-P curves. Regarding the P predictions, considering the Neo-Hookean term did not help either to improve the R^2 coefficients. This means that the circumferential mechanical response is dominated by the fiber behavior, which is consistent with similar results obtained recently on veins for instance [26].

Finally, the effect of testing conditions such as temperature has been assumed to be negligible but this needs to be confirmed. Moreover, the axial stretch may not be perfectly uniform in all the specimens due to 'end effects'. End effects occur in tensile tests when the length/diameter

ratio is low. This is the case of most of the specimens tested in this study and this may affect the P vs λ_θ behaviour, which may explain the low coefficients of determination reported in Table 2 for some specimens.

Further validation of the key findings in this study will employ a larger number of experimental tests for providing confirmation of these original results and offering a strong foundation for suggesting implications regarding the development of vascular disorders, the adaptation to alterations, and the extension to human arteries.

5. Conclusions

In this paper, we have proposed a simple biomechanical model and demonstrated it can predict the specific relationship between axial force and internal pressure for pig renal arteries and for other experimental results reported in the literature.

Several implications of the model predictions have been highlighted in the process of presenting the findings. For the homeostasis condition where the axial force is independent of the applied pressure, our results indicate that it is fully controlled by the orientation angle of helical collagen fibers. Therefore, the deposition of collagen fibers in arteries has a direct impact on this homeostasis condition as the axial force can only remain independent of the applied pressure if the average angle is preserved.

7.   References.

1. Avril, S., P. Badel, A. Duprey. Anisotropic and hyperelastic identification of in vitro human arteries from full-field measurements. J. Biomech. 43:2978–2985, 2010.

2. Badel, P., S. Avril, S. Lessner, M. Sutton. Mechanical identification of layer-specific properties of mouse carotid arteries using 3D-DIC and a hyperelastic anisotropic constitutive model. Comp Methods Biomech Biomed Eng. 15(1):37-48, 2012.

3. Brossollet, L.J., R.P. Vito. An alternate formulation of blood vessel mechanics and the meaning of the in vivo property. J. Biomech. 28:679–687, 1995.

4. Cardamone, L., A. Valentín, J.F. Eberth, J.D. Humphrey. Origin of axial prestretch and residual stress in arteries. Biomech Model Mechanobiol. 8(6):431-446, 2009.

5. Fung, Y.C. Biomechanics: Motion, Flow, Stress, and Growth. Springer: NY, 1990.

6. Gasser, T.C., R.W. Ogden, G.A. Holzapfel. Hyperelastic modelling of arterial layers with distributed collagen fibre orientations. J. R. Soc. Interface. 3(6):15-35, 2006.

7. Gleason, R.L., J.D. Humphrey. Effect of a sustained extension on arterial growth and remodeling: a theoretical study. J. Biomech. 40(4):1255-1261, 2005.

8. Gleason, R.L., E. Wilson, J.D. Humphrey. Biaxial biomechanical adaptations of mouse carotid arteries cultured at altered axial extension. J. Biomech. 38(6):766-776, 2007.

9. Hariton, I., G. deBotton, T.C. Gasser, G.A. Holzapfel. Stress-driven collagen fiber remodeling in arterial walls. Biomech. Model. Mechanobiol. 6:163–175, 2007.

10. Haskett, D., G. Johnson, A. Zhou, U. Utzinger, J. van de Geest. Microstructural and biomechanical alterations of the human aorta as a function of age and location. Biomech. Model. Mechanobiol. 9:725–736, 2010.

11. Hill, M.R., X. Duan, G.A. Gibson, S. Watkins, A.M. Robertson. A theoretical and non-destructive experimental approach for direct inclusion of measured collagen orientation and recruitment into mechanical models of the artery wall. J. Biomech., in press, 2012.

12. Holzapfel, G.A., T.C. Gasser, R.W. Ogden. A new constitutive framework for arterial wall mechanics and a comparative study of material models. J. Elast. 61:1–48, 2000.

13. Holzapfel, G.A. Determination of material models for arterial walls from uniaxial extension tests and histological structure. J. Theor. Biol. 238:290–302, 2006.

14. Hu, J.J., T.W. Fossum, M.W. Miller, H. Xu, J.C. Liu, J.D. Humphrey. Biomechanics of the porcine basilar artery in hypertension. Ann. Biomed. Eng. 35(1):19-29, 2007.

15. Humphrey, J.D. Cardiovascular Solid Mechanics: Cells, Tissues, and Organs. Springer: NY, 2002.

16. Humphrey, J.D., J.F. Eberth, W.W. Dye, R.L. Gleason. Fundamental role of axial stress in compensatory adaptations by arteries. J. Biomech. 42:1–8, 2009

17. Humphrey, J.D., K.R. Rajagopal. A constrained mixture model for arterial adaptations to a sustained step change in blood flow. Biomech. Model Mechanobiol. 2:109–126, 2003.

18. Kim, J.H., S. Avril, A. Duprey, J.P. Favre. Experimental characterization of rupture in human aortic aneurysms using a full-field measurement technique. Biomech. Model. Mechanobiol. In press, 2011.

19. Rachev, A. A model of arterial adaptation to alterations in blood flow. J. Elast. 61:83–111, 2000.

20. Sacks, M.S. Biaxial mechanical evaluation of planar biological materials. J. Elast. 61:199–246, 2000.

21. Valentín, A., L. Cardamone, S. Baek, J.D. Humphrey. Complementary vasoactivity and matrix remodeling in arterial adaptations to altered flow and pressure. J. R. Soc. Interface. 6:293-306, 2009.

22. Van de Geest J, M.S. Sacks, D. Vorp. Age dependency of the biaxial biomechanical behavior of human abdominal aorta. J Biomech Eng.126(6):815–822, 2004.

23. Van de Geest J, M.S. Sacks, D. Vorp. A planar biaxial constitutive relation for the luminal layer of intraluminal thrombus in abdominal aortic aneurysms. J Biomech. 39(13):2347–2354, 2006.

24. Van Loon, P., W. Klip, E.L. Bradley. Length–force and volume–pressure relationships of arteries. Biorheology 14:181–201, 1977.

25. Weizsacker, H.W., H. Lambert, K. Pascale. Analysis of the passive mechanical properties of rat carotid arteries. J. Biomech. 16:703–715, 1983.

26. McGilvray, K.C., R. Sarkar, K. Nguyen, C.M. Puttlitz. A biomechanical analysis of venous tissue in its normal and post-phlebitic conditions. J. Biomech. 43(15):2941–2947, 2010.

27. Baek, S., R.L. Gleason, K.R. Rajagopal, J.D. Humphrey JD. Theory of small on large: Potential utility in computations of fluid–solid interactions in arteries. Comput Methods Appl Mech Engrg. 196:3070–3078, 2007.

28. Masson, I., P. Boutouyrie, S. Laurent, J.D. Humphrey, M. Zidi. Characterization of arterial wall mechanical behavior and stresses from human clinical data. J. Biomech. 41:2618–2627, 2008.

29. Karšaj I., J.D. Humphrey. A Multilayered Wall Model of Arterial Growth and Remodeling. Mech Mater. 44:110-119, 2012.

List of tables

List of figures and Figure captions

Figure 1: Schematic of the cylindrical segment of artery and the loading system (in dotted lines, schematic of the helically arranged fibers).

Figure 2: Schematic of a network of fibers with two symmetric orientations.

Figure 3: Diagram defining the opening angle. It is known that the "traction-free" state in which the artery is excised from the body is not a stress-free state. Thus the arterial ring springs open when cut in a radial direction. It is assumed that the open sector is the undeformed stress-free reference configuration. No axial deformation is assumed to occur during radial separation, so that the axial stretch between the stress-free to traction-free state is approximated to 1.

Figure 4: Pictures of the experimental test performed on the segments of artery. (a) Environmental chamber in Bose test bench and vertically oriented camera; (b) representative example of porcine renal artery attached to barbed Luer fixtures inside environmental chamber for mechanical testing. Scale bar in mm.

Figure 5: F-P curves obtained on two different specimens (experiment and model):

(a): RRA on pig ID#5, coefficient of determination R^2=0.59

(b): LSA2 on pig ID#3, coefficient of determination R^2=0.87

Figure 6: P vs λ_θ curves obtained on two different specimens (experiment and model):

(a): RRA on pig ID#5, coefficient of determination R^2=0.65

(b): LSA2 on pig ID#3, coefficient of determination R^2=0.7

Figure 7: σ_{zz} vs λ_z curves obtained on two different specimens (experiment and model):

(a): RRA on pig ID#5, coefficient of determination R^2=0.96

(b): LSA2 on pig ID#3, coefficient of determination R^2=0.85

Figure 8: Qualitative comparison between experimental data obtained for a pig basilar artery [14] and our model for the same artery.

(a) Experimental force vs pressure curves obtained for a pig basilar artery [14]

(b) Theoretical force vs pressure curves obtained with Eq. (11) for the same artery

Appendix

Let $\underline{e}_{\Phi_0}$ denote a unit vector in the stress-free configuration defined such that:

$$\{\underline{e}_{\Phi_0}\} = \left\{ \begin{array}{c} 0 \\ \cos(\Phi_0) \\ \sin(\Phi_0) \end{array} \right\} \tag{A1}$$

Due to the deformation, this vector is transformed as follows:

$$\{\underline{e}_\Phi\} = [\underline{F}] \{\underline{e}_{\Phi_0}\} = \left\{ \begin{array}{c} 0 \\ \lambda_\theta \cos(\Phi_0) \\ \lambda_z \sin(\Phi_0) \end{array} \right\} = \left\{ \begin{array}{c} 0 \\ \lambda_{\Phi_0} \cos(\Phi) \\ \lambda_{\Phi_0} \sin(\Phi) \end{array} \right\} \tag{A2}$$

where: $\lambda_{\Phi_0}^2 = \lambda_\theta^2 \cos^2(\Phi_0) + \lambda_z^2 \sin^2(\Phi_0)$ is the stretch in the direction aligned at an angle Φ_0 in the stress-free configuration.

This means that a vector aligned at an angle Φ_0 in the stress-free configuration is transformed into a vector aligned at an angle Φ such that:

$$\tan(\Phi) = \tan(\Phi_0) \, [\lambda_z / \lambda_\theta] \tag{A3}$$

Denoting the initial fiber orientations of the model as $+\beta_0$ and $-\beta_0$ (stress-free configuration) for the helically arranged fibers, and considering fiber rotation to an angle $+\beta$ and $-\beta$ during mechanical loading, the following expression is obtained relating β_0 and β:

$$\tan^2(\beta) = \tan^2(\beta_0) \, [\lambda_z^2 / \lambda_\theta^2] \tag{A4}$$

The strain energy function considered in this study may be written as:

$$\Psi = \rho_0 \Psi_0 + \rho_{90} \Psi_{90} + \rho_\beta \Psi_\beta + \rho_m \Psi_m \tag{A5}$$

Where ρ_Φ denotes the volume fraction of the fibers oriented at angle ϕ and ψ_ϕ denotes the strain energy function of the fibers oriented at angle ϕ (Note that $\rho_\beta \psi_\beta$ represents the contribution of fibers at β_0 and $-\beta_0$), ρ_m denotes the volume fraction of the matrix and ψ_m is the strain energy function of the matrix (NeoHookean type).

In this study, we use the following form of strain energy function for the fibers:

$$\rho_\phi \Psi_\phi = \frac{k_{\phi 1}}{4k_{\phi 2}} \left[\exp\left(k_{\phi 2} \left(\lambda_\phi^2 - 1 \right)^2 \right) - 1 \right] \tag{A6}$$

Assuming incompressibility, the Cauchy stress tensor may be written:

$$\underline{\underline{\sigma}} = \underline{\underline{F}} \frac{\partial \Psi}{\partial \underline{\underline{E}}} \underline{\underline{F}}^T + c\underline{\underline{I}} \tag{A7}$$

Where $\underline{\underline{F}}$ is the deformation gradient tensor, $\underline{\underline{E}}$ is the Green-Lagrange strain tensor, c is a scalar and $\underline{\underline{I}}$ is the identity tensor.

It can be derived:

$$\left[\frac{\partial \rho_\phi \Psi_\phi}{\partial \underline{\underline{E}}} \right] = \begin{bmatrix} 0 & 0 & 0 \\ 0 & \cos^2(\phi) & 0 \\ 0 & 0 & \sin^2(\phi) \end{bmatrix} k_{\phi 1} \left(\lambda_\phi^2 - 1 \right) \exp\left(k_{\phi 2} \left(\lambda_\phi^2 - 1 \right)^2 \right) \tag{A8}$$

So:

$$\left[\underline{\underline{F}} \frac{\partial \rho_0 \Psi_0}{\partial \underline{\underline{E}}} \underline{\underline{F}}^T \right] = \begin{bmatrix} 0 & 0 & 0 \\ 0 & 1 & 0 \\ 0 & 0 & 0 \end{bmatrix} \rho_0 \sigma_0 \text{ with: } \rho_0 \sigma_0 = k_{01} \left(\lambda_\theta^2 - 1 \right) \exp\left(k_{02} \left(\lambda_\theta^2 - 1 \right)^2 \right) \lambda_\theta^2 \tag{A9}$$

$$\left[\underline{\underline{F}} \frac{\partial \rho_{90} \Psi_{90}}{\partial \underline{\underline{E}}} \underline{\underline{F}}^T \right] = \begin{bmatrix} 0 & 0 & 0 \\ 0 & 0 & 0 \\ 0 & 0 & 1 \end{bmatrix} \rho_{90} \sigma_{90} \text{ with: } \rho_{90} \sigma_{90} = k_{901} \left(\lambda_z^2 - 1 \right) \exp\left(k_{902} \left(\lambda_z^2 - 1 \right)^2 \right) \lambda_z^2 \tag{A10}$$

$$\left[\underline{\underline{F}}\frac{\partial\rho_{\beta_0}\Psi_{\beta_0}}{\partial\underline{\underline{E}}}\underline{\underline{F}}^T\right]=\begin{bmatrix}0 & 0 & 0 \\ 0 & \dfrac{\lambda_\theta^2}{\lambda_{\beta_0}^2}\cos^2(\beta_0) & 0 \\ 0 & 0 & \dfrac{\lambda_z^2}{\lambda_{\beta_0}^2}\sin^2(\beta_0)\end{bmatrix}\rho_\beta\sigma_\beta=\begin{bmatrix}0 & 0 & 0 \\ 0 & \cos^2(\beta) & 0 \\ 0 & 0 & \sin^2(\beta)\end{bmatrix}\rho_\beta\sigma_\beta \quad \text{(A11)}$$

with : $\rho_\beta\sigma_\beta = k_{\beta 1}\left(\lambda_{\beta_0}^2 - 1\right)\exp\left(k_{\beta 2}\left(\lambda_{\beta_0}^2 - 1\right)^2\right)\lambda_{\beta_0}^2$ (A12)

$$\left[\underline{\underline{F}}\frac{\partial\rho_m\Psi_m}{\partial\underline{\underline{E}}}\underline{\underline{F}}^T\right]=2C_{10}\begin{bmatrix}\lambda_\theta^{-2}\lambda_z^{-2} & 0 & 0 \\ 0 & \lambda_\theta^2 & 0 \\ 0 & 0 & \lambda_z^2\end{bmatrix} \quad \text{(A13)}$$

Eventually, the whole Cauchy stress for the material model of this study may be written:

$$\underline{\underline{\sigma}}=\begin{bmatrix}0 & 0 & 0 \\ 0 & \cos^2(\beta) & 0 \\ 0 & 0 & \sin^2(\beta)\end{bmatrix}\rho_\beta\sigma_\beta+\begin{bmatrix}0 & 0 & 0 \\ 0 & 1 & 0 \\ 0 & 0 & 0\end{bmatrix}\rho_0\sigma_0+\begin{bmatrix}0 & 0 & 0 \\ 0 & 0 & 0 \\ 0 & 0 & 1\end{bmatrix}\rho_{90}\sigma_{90}+2C_{10}\begin{bmatrix}\lambda_\theta^{-2}\lambda_z^{-2} & 0 & 0 \\ 0 & \lambda_\theta^2 & 0 \\ 0 & 0 & \lambda_z^2\end{bmatrix}+c\underline{\underline{I}}$$

(A14)

Finally, the following equations can be derived:

$$\begin{aligned}\sigma_{\theta\theta}-\sigma_{rr} &= \rho_\beta\cos^2(\beta)\sigma_\beta + \rho_0\sigma_0 + 2C_{10}\left[\lambda_\theta^2 - \lambda_\theta^{-2}\lambda_z^{-2}\right] \\ \sigma_{zz}-\sigma_{rr} &= \rho_\beta\sin^2(\beta)\sigma_\beta + \rho_{90}\sigma_{90} + 2C_{10}\left[\lambda_z^2 - \lambda_\theta^{-2}\lambda_z^{-2}\right]\end{aligned}$$

(A15)

Neglecting the NeoHookean contribution, one obtains:

$$\begin{aligned}\sigma_{\theta\theta}-\sigma_{rr} &= \cos^2(\beta)\rho_\beta\sigma_\beta + \rho_0\sigma_0 \\ \sigma_{zz}-\sigma_{rr} &= \sin^2(\beta)\rho_\beta\sigma_\beta + \rho_{90}\sigma_{90}\end{aligned}$$

(A16)

Feeding Eq. 2 with the derived stress expressions, the prediction of the pressure is:

$$\tilde{P} = \int_{r_i}^{r_o}\left[\sigma_{\theta\theta}(r) - \sigma_{rr}(r)\right]\frac{dr}{r}$$

$$\tilde{P} = \int_{r_i}^{r_o}\left[\cos^2(\beta)\rho_\beta\sigma_\beta + \rho_0\sigma_0\right]\frac{dr}{r}$$

(A17)

$$\tilde{P} = \int_{r_i}^{r_o}\left[k_{\beta 1}\lambda_\theta^2\cos^2(\beta_0)\left(\lambda_{\beta_0}^2 - 1\right)\exp\left(k_{\beta 2}\left(\lambda_{\beta_0}^2 - 1\right)^2\right) + k_{01}\lambda_\theta^2\left(\lambda_\theta^2 - 1\right)\exp\left(k_{02}\left(\lambda_\theta^2 - 1\right)^2\right)\right]\frac{dr}{r}$$

Feeding Eq. 1 with the derived stress expressions, the prediction of the axial force is:

28

$$\tilde{F}_z = 2\pi \int_{r_i}^{r_o} \sigma_{zz}(r)\,r\,dr - \pi r_i^2 P$$

(A18)

$$\tilde{F}_z = 2\pi \int_{r_i}^{r_o} [\sigma_{zz}(r) - \sigma_{rr}(r)]\,r\,dr + 2\pi \int_{r_i}^{r_o} \sigma_{rr}(r)\,r\,dr - \pi r_i^2 P$$

It is recalled that:

$$\sigma_{rr}(r) = -\int_{r}^{r_o} [\sigma_{\theta\theta}(\xi) - \sigma_{rr}(\xi)]\frac{d\xi}{\xi}$$

(A19)

$$\sigma_{rr}(r) = -\int_{r}^{r_o} \left[k_{\beta 1}\lambda_\theta^2 \cos^2(\beta_0)\left(\lambda_{\beta_0}^2 - 1\right)\exp\left(k_{\beta 2}\left(\lambda_{\beta_0}^2 - 1\right)^2\right) + k_{01}\lambda_\theta^2\left(\lambda_\theta^2 - 1\right)\exp\left(k_{02}\left(\lambda_\theta^2 - 1\right)^2\right) \right]\frac{d\xi}{\xi}$$

So $\sigma_{rr}(r)$ varies from –P to 0 for r varying between r_i and r_o.

It means that there exists a radius value, denoted r_a, such as: $r_i < r_a < r_o$ and:

$$\int_{r_i}^{r_o} \sigma_{rr}(r)\,r\,dr = -\int_{r_i}^{r_a} P\,r\,dr = -\frac{1}{2}P\left(r_a^2 - r_i^2\right)$$

(A20)

Eventually:

$$\tilde{F}_z = 2\pi \int_{r_i}^{r_o} [\sigma_{zz}(r) - \sigma_{rr}(r)]\,r\,dr - \pi r_a^2 P$$

(A21)

$$\tilde{F}_z = \tilde{F}_0(\lambda_z) + \int_{r_i}^{r_o} 2\pi\left[k_{\beta 1}\lambda_z^2 \sin^2(\beta_0)\left(\lambda_{\beta_0}^2 - 1\right)\exp\left(k_{\beta 2}\left(\lambda_{\beta_0}^2 - 1\right)^2\right) \right] r\,dr - P\pi r_a^2$$

The value of r_a is calibrated by running repetitively the identification of the material properties. At the first run, it is assumed: $r_a = r_i + h/2$, where $h = r_o - r_i$. Then, at the next iteration, for each load step, using Eq. (A20), it can be written:

$$r_a^2 = r_i^2 + \frac{2}{P}\int_{r_i}^{r_o}\left(\int_{r}^{r_o}\left[k_{\beta 1}\lambda_\theta^2 \cos^2(\beta_0)\left(\lambda_{\beta_0}^2 - 1\right)\exp\left(k_{\beta 2}\left(\lambda_{\beta_0}^2 - 1\right)^2\right) + k_{01}\lambda_\theta^2\left(\lambda_\theta^2 - 1\right)\exp\left(k_{02}\left(\lambda_\theta^2 - 1\right)^2\right) \right]\frac{d\xi}{\xi} \right)r\,dr$$

(A22)

The identified values of the material properties vary less than 1% after 3 iterations of this repeated process.

Table 1: Measured dimensions of the tested arteries.

Pig ID	Specimen	Traction-free outer diameter (mm)	Traction-free length (mm)	α (°)	Thickness in the reference stress-free configuration (mm)
1	RRA	7.22	16.6	120	1.12
1	LSA	5.52	9.5	120	1.06
2	RRA	7.47	11.7	116	1.7
2	LSA	4.77	11	94	1.22
3	RRA	6.59	10.77	118	2.26
3	LSA	5.73	10.87	82	1.25
3	LSA	4.34	18.89	46	0.98
5	RRA	7.8	22.3	314	1.14
6	LRA	7.82	12.8	128	1.65
6	RRA	9.72	24.8	60	1.23

Table 2: Identified model parameters of the tested arteries.

Pig ID	Speci-men	$k_{\beta 1}$ (kPa)	$k_{\beta 2}$	β_0	k_{01} (kPa)	k_{02}	k_{901} (kPa)	k_{902}	R^2 of F-P	R^2 of P vs λ_θ	R^2 of F_0 vs λ_z
1	RRA	9.4	13.8	61°	0	0	15.7	8.2	0.91	0.75	0.87
1	LSA	61.6	4.4	65°	0	0	14.6	0.3	0.98	0.42	0.85
2	RRA	2.49	1.75	37°	0	0	121	4.4	0.81	0.36	0.85
2	LSA	69.5	3.3	55°	21.8	2.97	36.6	5.2	0.55	0.44	0.85
3	RRA	34.4	0.46	5°	0	0	2.98	27	0.97	0.24	0.79
3	LSA	203	0.04	5°	0	0	0.27	72	0.77	0.3	0.3
3	LSA	45.2	2.22	63°	6	0.45	87	0.1	0.87	0.7	0.80
5	RRA	19.7	2.6	49°	0	0	71.3	1.6	0.59	0.65	0.96
6	LRA	6220	0	5°	0	0	13.9	9.6	0.52	0.4	0.75
6	RRA	3780	0.13	80°	0.01	1.7	27.2	0.4	0.3	0.24	0.91
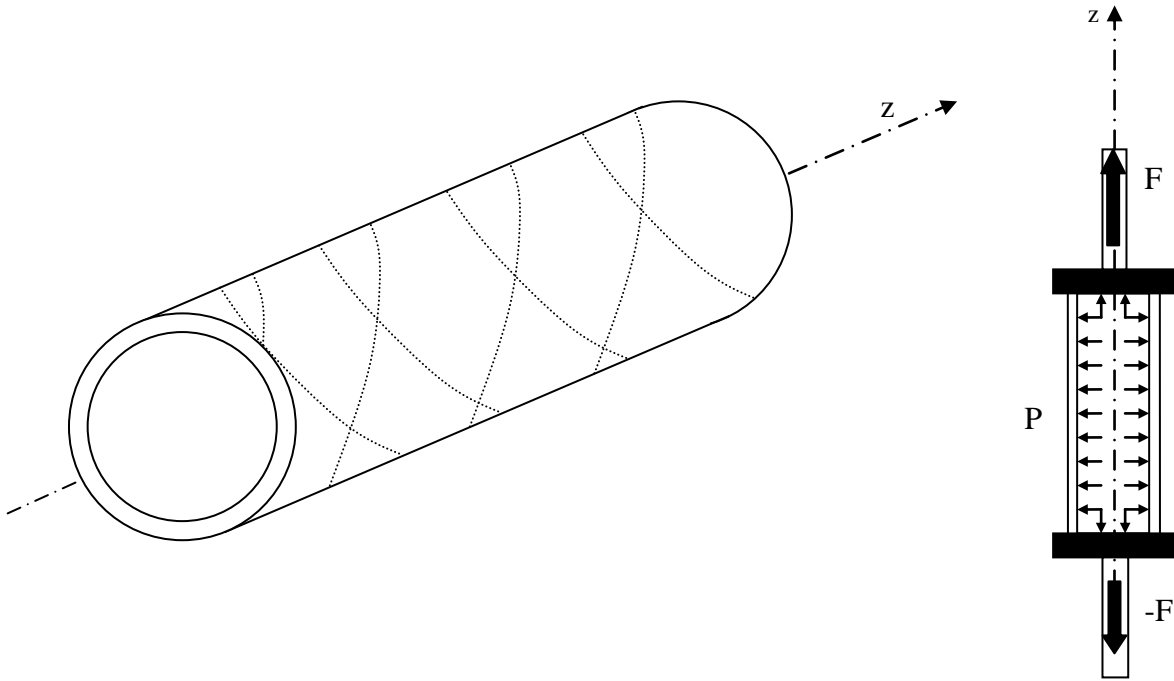
Figure 1

First author: Stéphane Avril
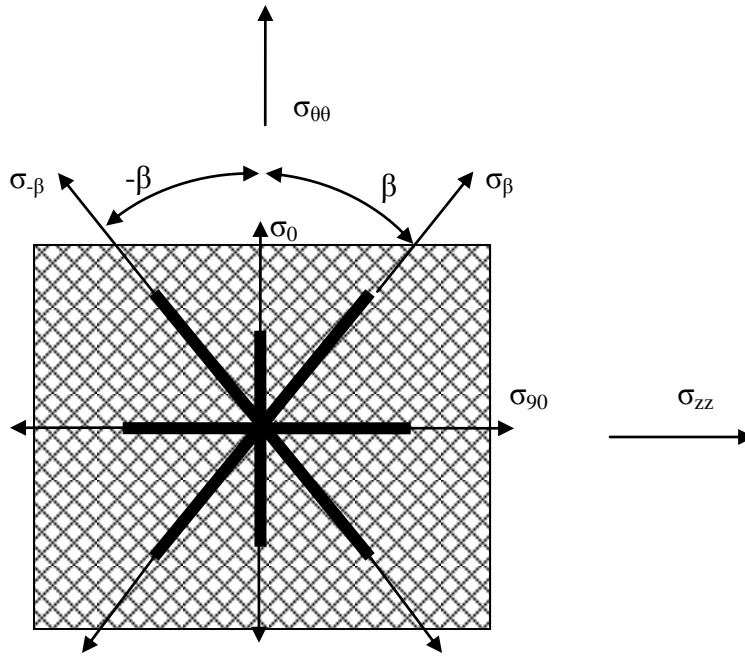
Figure 2

First author: Stéphane Avril
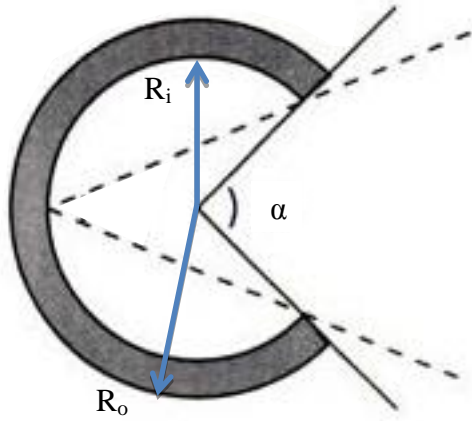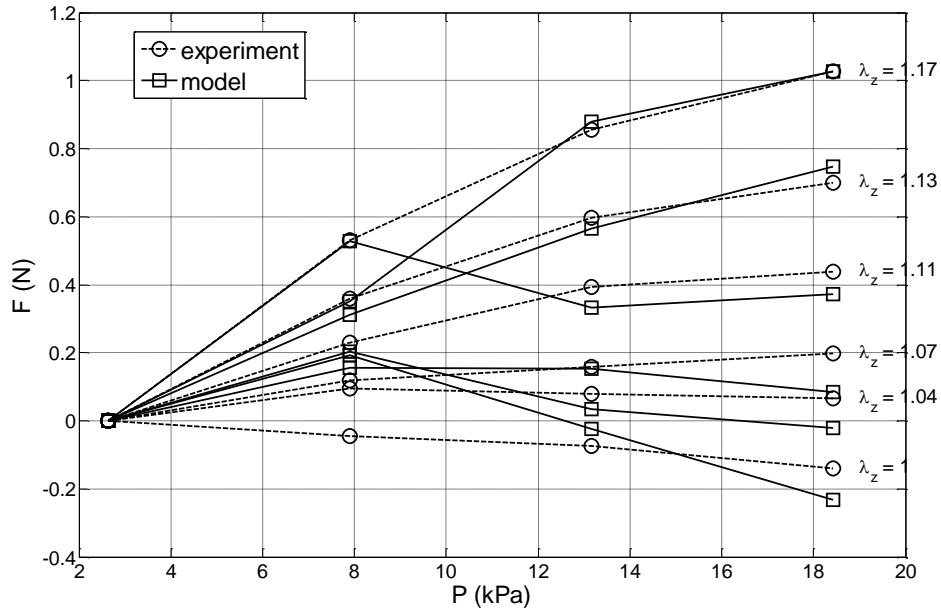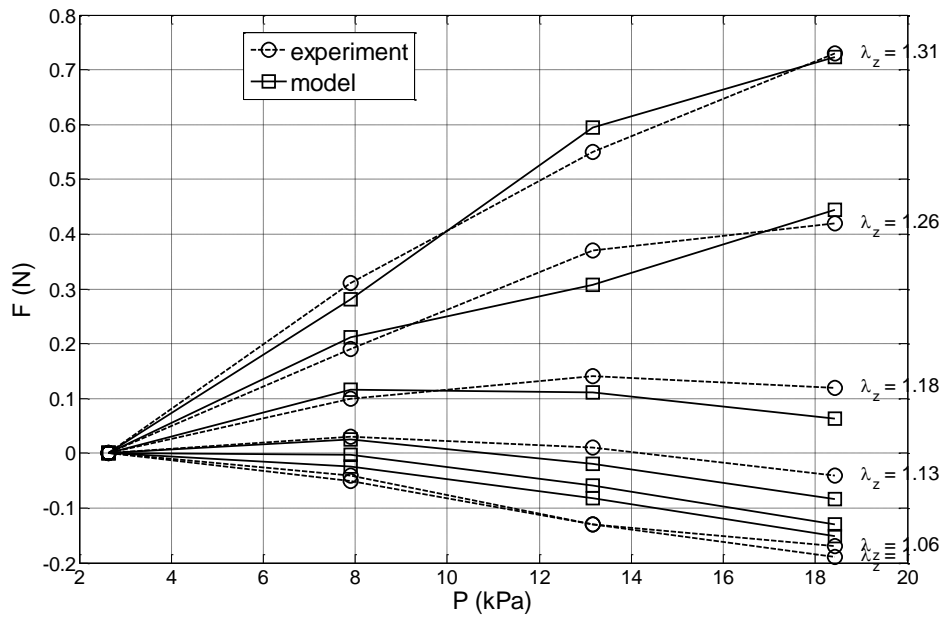
Figure 3

First author: Stéphane Avril

(a)
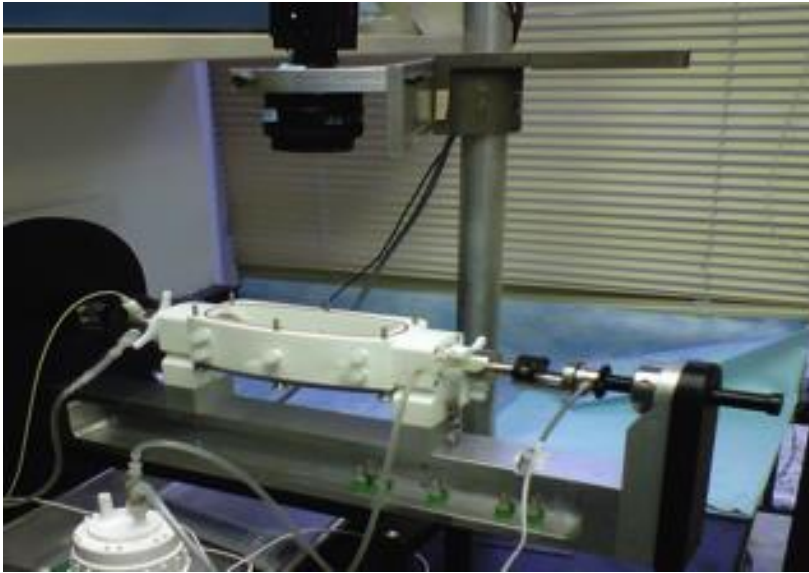
(b)
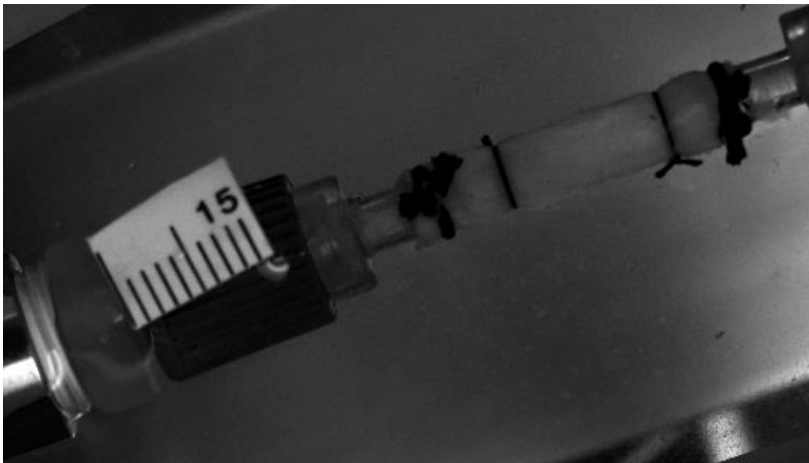
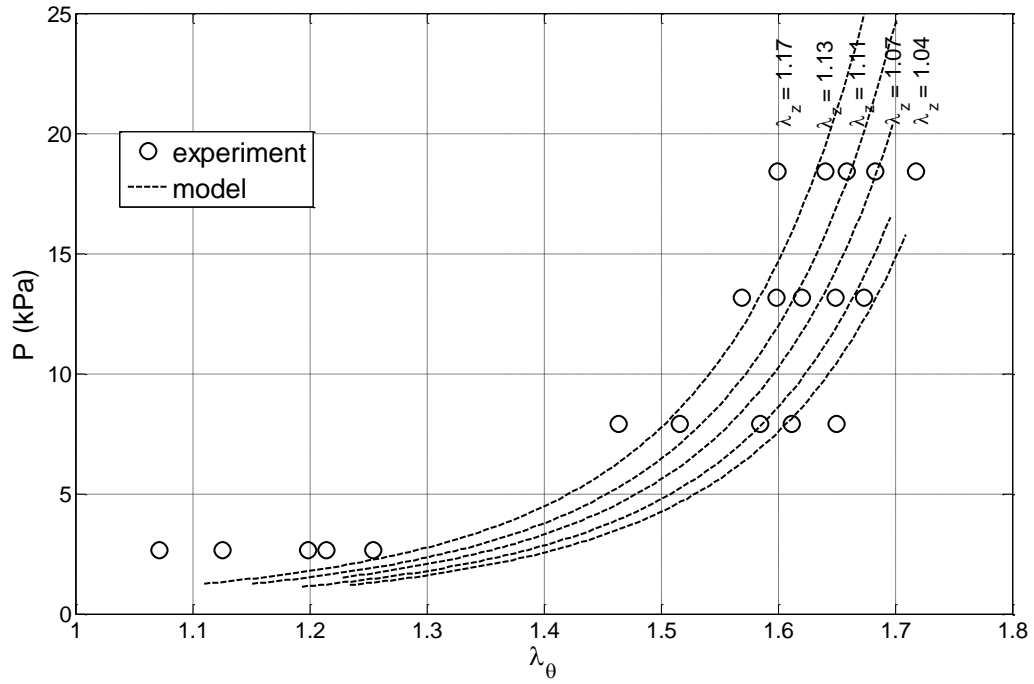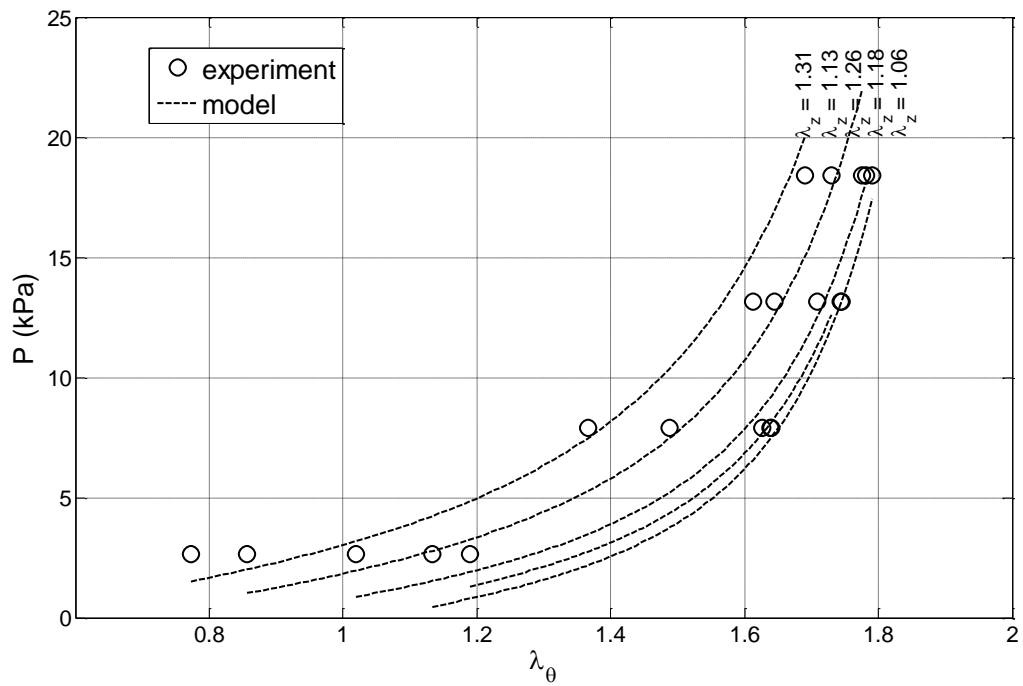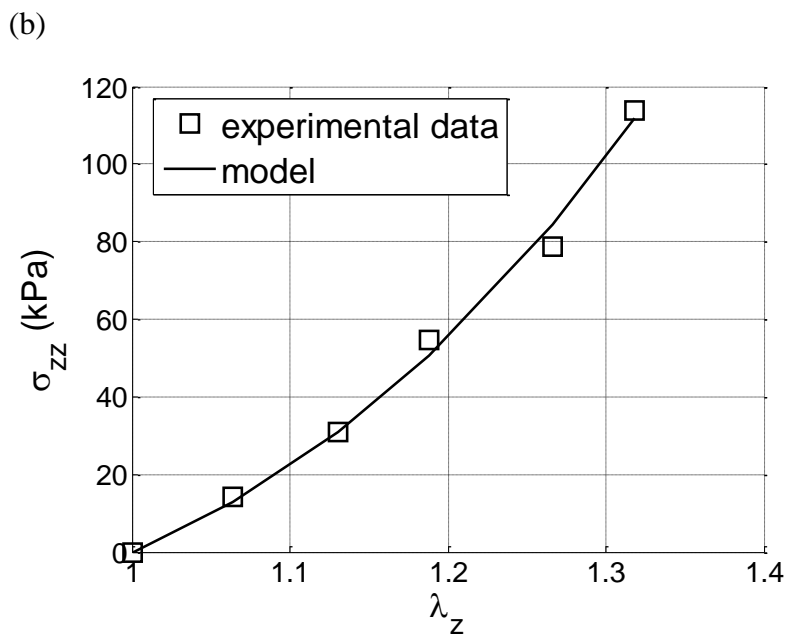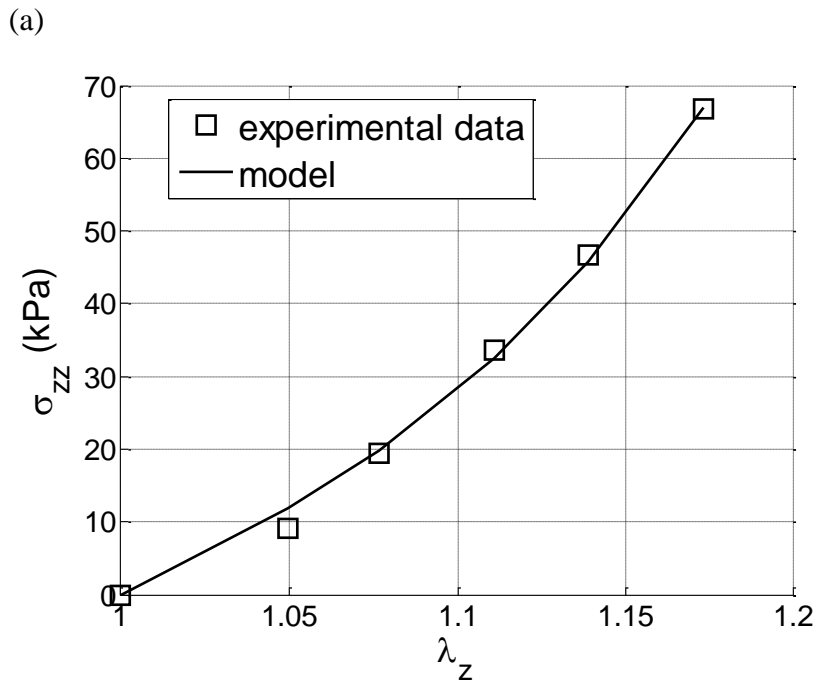

Figure 4

First author: Stéphane Avril

(a)

(b)

Figure 5

First author: Stéphane Avril

36

(a)

(b)

Figure 6

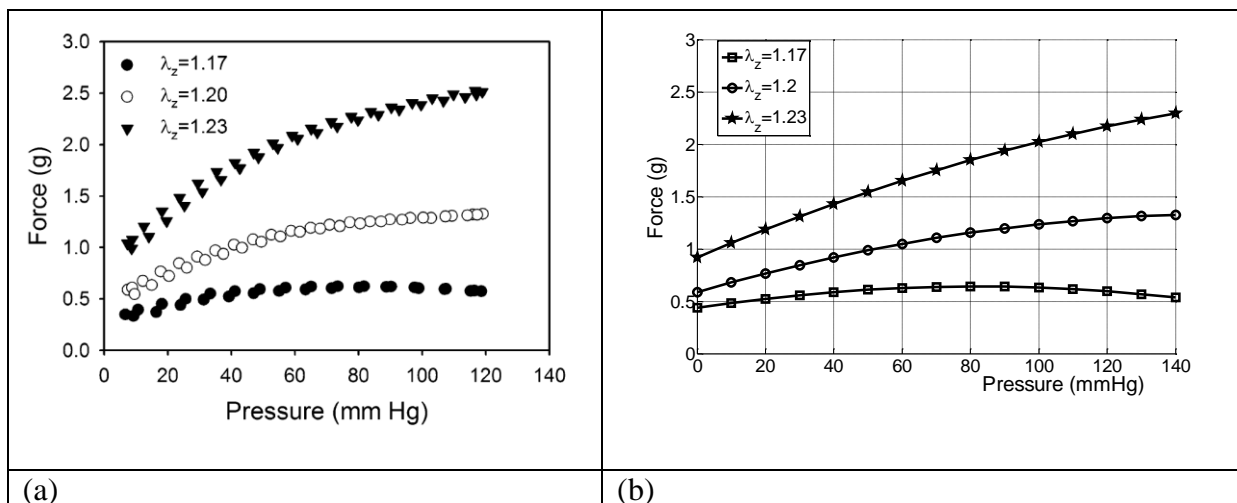First author: Stéphane Avril

(a)

(b)

Figure 7

First author: Stéphane Avril

Figure 8

First author: Stéphane Avril